

Compositional Control and Optimization of Molecular Beam Epitaxial Growth of $(\text{Sb}_2\text{Te}_3)_{1-x}(\text{MnSb}_2\text{Te}_4)_x$ Magnetic Topological Insulators

Ido Levy, Candice Forrester, Haiming Deng, Manuel Roldan-Gutierrez, Martha R. McCartney, David J. Smith, Christophe Testelin, Lia Krusin-Elbaum, and Maria C. Tamargo*



Cite This: *Cryst. Growth Des.* 2022, 22, 3007–3015



Read Online

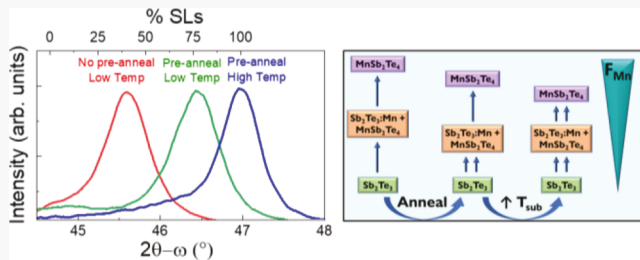
ACCESS |

Metrics & More

Article Recommendations

ABSTRACT: Magnetic topological insulators such as MnBi_2Te_4 and MnSb_2Te_4 are promising hosts of novel physical phenomena such as the quantum anomalous Hall effect and intrinsic axion insulator state, both potentially important for the implementation in topological spintronics and error-free quantum computing. In the bulk, the materials are antiferromagnetic, but appropriate stacking with nonmagnetic layers or excess Mn in the crystal lattice can induce a net ferromagnetic alignment. Accurate control of the materials growth is thus essential to optimize the magnetic properties. In this work, we report a detailed investigation of the

growth of $(\text{Sb}_2\text{Te}_3)_{1-x}(\text{MnSb}_2\text{Te}_4)_x$ layers with varying Mn content by molecular beam epitaxy. The Mn flux fraction provided during growth controls the percent of MnSb_2Te_4 that is formed in the resulting layers by a self-assembly process. Highly crystalline layers with compositions varying between Sb_2Te_3 ($x = 0$) and MnSb_2Te_4 ($x = 1$) were obtained. The results show that Mn is incorporated as a structural component to form septuple layers (SLs) of MnSb_2Te_4 . Excess Mn was observed in the samples, suggesting that it is incorporated as antisite defects into both Sb_2Te_3 and MnSb_2Te_4 . Two modifications of the growth conditions were implemented to enhance the incorporation of Mn as a structural element to form MnSb_2Te_4 SLs: annealing of a thin portion of the layer at the beginning of growth (*preannealing step*) and increasing the growth temperature. Both result in a larger percent of MnSb_2Te_4 SLs for similar Mn flux fractions during growth, increasing the control of the growth and providing insight into the Mn incorporation process.



INTRODUCTION

Incorporation of magnetic elements into 3D topological insulators (TIs) such as Bi_2Te_3 and Sb_2Te_3 has garnered a great deal of interest in recent years because of the potential to achieve the quantum anomalous Hall effect (QAHE)¹ and other exotic phenomena. The QAHE was first demonstrated by incorporating Cr as a dopant into thin $(\text{Bi},\text{Sb})_2\text{Te}_3$ films.² However, defects caused by the incorporation of the Cr atoms into the TI crystal lattice resulted in the effect being only evident at sub-Kelvin temperatures.^{3–6} Recently, it was discovered that adding Mn to Bi and Te or Sb and Te during growth leads to a formation of a new crystal phase, MnBi_2Te_4 or MnSb_2Te_4 , respectively, having a septuple layer (SL) structure rather than the typical quintuple layer (QL) structure of the nonmagnetic TIs.⁷ These intrinsically magnetic crystals, rather than magnetically doped TIs, may contain fewer defects and lead to improved properties. In these materials, a single SL is ferromagnetic, with the magnetic spins aligned out of plane. However, when stacked to form a bulk structure, the SLs couple antiferromagnetically and are not conducive to the observation of QAHE, except in the ultrathin layers of odd

number (5–7) of SLs.⁸ One approach used to resolve this problem was to separate the magnetic SL layers with a few nonmagnetic QLs, enabling ferromagnetic coupling between the nonadjacent SLs.⁹ Another approach shown to produce ferromagnetic coupling of the SLs in MnSb_2Te_4 was to introduce excess Mn into the pure SL structure. It has been proposed that Mn_{SL} antisite defects induce ferromagnetic coupling between the SLs.^{10–12}

The growth of MnSb_2Te_4 or of mixed SL:QL layered structures, has mostly been reported by bulk growth techniques, while only a few groups have explored epitaxial growth techniques for these compounds.^{13–14} In both methods of growth, the formation of SLs occurs by self-assembly

Received: December 9, 2021

Revised: March 12, 2022

Published: March 31, 2022



depending on the amount of Mn provided during growth. Typically, to grow these materials, all the elements are mixed simultaneously to form the crystal, and the resulting mix of SLs and QLs depends on the amount of Mn added. Although self-assembly is a convenient method to grow these materials because of its simplicity, it has some important drawbacks, particularly the difficulty in controlling the formation of a specific structure or composition reproducibly and consistently throughout the crystal lattice. Molecular beam epitaxy (MBE) with its layer-by-layer growth mechanism promises to provide certain benefits for control of the desired structures. Several groups have reported some specifics of the MBE growth for Bi-based magnetic TIs,^{15–17} while much less work has been reported for MnSb₂Te₄-based materials.^{12,18} In general, very little work has yet been done to systematically investigate and understand the MBE growth process and the parameters that affect and control the structural properties of the resulting magnetic TIs. Such an understanding is essential for the intentional growth of precise layered structures with accurate compositional control and the desired magnetic properties. For example, inserting precise numbers of nonmagnetic TI QLs between magnetic TI SLs, which remains a significant challenge, has the potential to achieve intrinsic 3D magnetic TIs with a gap opening in the surface state band,¹⁹ as was seen in MnBi₂Se₄/Bi₂Se₃^{18,19} or MnBi₂Te₄/Bi₂Te₃.^{18,20}

In this work, we perform a detailed investigation of the growth of $(\text{Sb}_2\text{Te}_3)_{1-x}(\text{MnSb}_2\text{Te}_4)_x$ structures by MBE. Variation of the Mn flux during growth enables control of the SL to QL ratio in the layer. We find that competing processes, such as Mn dopant incorporation into the QL and excess Mn in the SLs, introduce inaccuracies in the control of the SL to QL layer ratio. Moreover, the distribution of the SLs throughout the crystal is random so that the local properties of the material vary. Modified growth techniques, involving the implementation of a *preannealing step* in the early stages of growth and the increase of the growth temperature, are explored. We observe a preferential incorporation of Mn into SLs and an improved structural quality resulting from these changes. A mechanism is proposed to explain the observed improvements in the control of the growth and the material properties, which also provides insight as for the Mn incorporation process. We propose that this improved understanding of the MBE growth process will lead to the ability to perform on-demand growth of specific well-ordered structures with accurate control of the Mn composition¹² or the insertion of precise numbers of nonmagnetic TI interlayers between the magnetic SLs to achieve the desired interlayer coupling.^{9,21,22} Such control of the growth will enable true breakthroughs in the magnetic behavior of the materials.

■ EXPERIMENTAL SECTION

All samples were grown in a Riber 2300P system with a base pressure of 3.5×10^{-10} Torr, equipped with reflection high-energy electron diffraction (RHEED) for *in situ* growth monitoring, on epi-ready *c*-plane (0001) sapphire substrates. The substrates were heated under vacuum to 600 °C for 1 h prior to growth to remove impurities from the surface. High-purity 6 N antimony (Sb), tellurium (Te), and 5 N 8 manganese (Mn) fluxes were achieved using a Riber double zone cell for Sb and single-zone Knudsen cells for Mn and Te. The fluxes were measured by the beam equivalent pressure (BEP) read by an ion gauge placed in the position of the substrate prior to growth. The Mn BEP ratio, $\text{BEP}(\text{Mn})/[\text{BEP}(\text{Mn}) + \text{BEP}(\text{Sb})]$, proportional to the Mn flux fraction, was used to control the Mn content during growth and was varied between 0.00 and 0.11. Growth was performed under

excess Te flux. The samples were grown by MBE via a two-step growth method consisting of an initial deposition of a thin (usually 3–5 nm) low-temperature buffer (LTB) Sb₂Te₃ layer, at 200 °C for ~3 to 5 min. The LTB layer growth was then stopped, while keeping constant Te flux at the sample surface, and the substrate temperature was raised to the desired growth temperature of 245–255 °C. An LTB growth has been shown to improve nucleation in MBE growth of TIs.^{23,24} Next, the Mn-containing layer was grown for 1–2 h, during which the Mn, Sb, and Te sources were simultaneously impinging on the sample surface. The Te/Sb BEP ratios were kept between 20 and 30, ensuring excess Te during growth. All samples used similar Sb flux, and the composition was varied by adjusting the Mn cell temperature to change the Mn flux. The growth rates for the samples varied between 0.4 and 1.2 nm/min depending on the amount of Mn incorporated.

All samples were characterized by a variety of postgrowth techniques. High-resolution X-ray diffraction (HR-XRD) measurements were performed using a Bruker D8 Discover diffractometer with a da Vinci configuration and a Cu K α 1(1.5418 Å) source. Atomic force microscopy (AFM) images were obtained using a Bruker Dimension FastScan AFM with a FastScan-A silicon probe. Scanning transmission electron microscopy (STEM) images (Figure 2a–d) were obtained (EAG Laboratories) using a Hitachi HD-2700 spherical aberration-corrected scanning-TEM system coupled with energy-dispersive X-ray spectroscopy (EDX). Further high-resolution STEM imaging (Figure 6) was carried out using a probe-corrected JEOL ARM-200F operated at 200 keV. Hall transport measurements were performed in a 14 T quantum design physical property measurement system in 1 mTorr (at low temperature) of He gas. Electrical contacts in the vdp configuration were made with indium bonded on the edge of the thin film.

■ RESULTS AND DISCUSSION

Growth was monitored *in situ* by RHEED. Typical patterns at the end of the growth and AFM surface images are shown in Figure 1. The initial RHEED pattern after the LTB and during

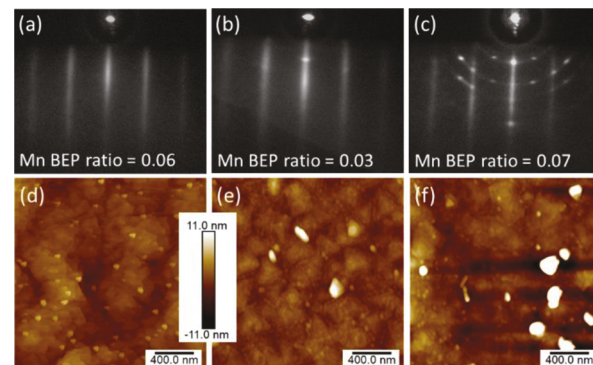


Figure 1. *In situ* RHEED images (a–c) of three samples and their corresponding $2 \mu\text{m} \times 2 \mu\text{m}$ AFM (d–f) images. The Mn BEP ratios for each sample are noted in the RHEED images. All AFM images are based on the same scale bar, shown between panels (d) and (e).

initiation of growth often exhibited some polycrystalline rings or spotty features which typically disappeared or became less prominent as the growth proceeded. Figure 1a–c show the RHEED images taken at the end of the growth for three samples grown with different Mn BEP ratios. Most samples, regardless of composition, showed a streaky pattern, such as the one shown in Figure 1a; however, a few samples exhibited additional features suggesting rough surfaces and some disorder, as illustrated in Figure 1b,c. A corresponding variation in surface roughness is also visible in the AFM images presented in Figure 1d–f.

STEM observations were made for some of the samples using HAADF imaging because of its high-Z sensitivity. Figure 2 compares HAADF STEM cross sections of two samples

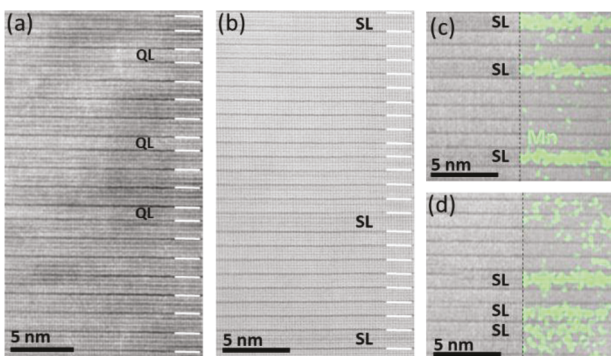


Figure 2. High-angle annular-dark-field (HAADF) STEM images of two samples grown with different Mn BEP ratios, 0.10 and 0.02 for (a) and (b), respectively. The van der Waals gaps are marked by short white lines, and the difference in thicknesses of SLs and QLs is easily discernible. (a) Sample containing 27.4% Mn (obtained from EDX measurements) and 71% SLs; (b) sample containing 8.1% Mn and 13% SLs. (c,d) Cross-sectional EDX scan of Mn (green) overlaid on two different regions of the TEM image from the sample shown in panel (b).

containing low and high Mn levels. The relatively low magnification STEM images presented in Figure 2a,b enabled the analysis of large regions of each sample from which estimates for the relative amount of septuple layers (%SL) could be made. The results illustrate the formation of SLs and QLs in different proportions, 71% SLs in Figure 2a and 13% SLs in Figure 2b. The STEM images show well-ordered, highly crystalline structures and no obvious defects. The sample shown in Figure 2a, which was grown using an Mn BEP fraction of 0.10, has a crystal structure that consists of mostly SLs, 71% calculated from the STEM image, and has a 27.4% Mn atomic percent, as obtained from EDX. Because pure stoichiometric MnSb_2Te_4 contains 14% Mn, this result implies that the sample contains a great deal of excess Mn incorporated into the layer without resulting in SLs. Thus we conclude that although some of the Mn incorporated to form the SL structure, a significant amount of Mn must also be incorporated as an impurity in the SLs and the QLs in that sample. Figure 2b shows the STEM image for a sample that contains only 13% SLs and has a Mn content of 8.1% (from EDX). As for the previous sample, based on the Mn content obtained from EDX, a higher amount of SLs (over 50%) would be expected if all the Mn atoms were incorporated to form stoichiometric SLs, suggesting again the incorporation of Mn as an impurity in the structure. The presence of excess Mn throughout the sample can be seen in Figure 2c,d, which shows the Mn EDX cross-sectional scan overlaid on the STEM image in two different regions of the sample of Figure 2b. The EDX data show that, in the region depicted in Figure 2c the Mn is largely contained in the SLs, whereas in the region of Figure 2d the Mn atoms are more randomly distributed throughout the crystal lattice. This result suggests that during growth, the Mn is initially incorporated as a dopant impurity into Sb_2Te_3 without modifying the crystal structure, that is, not forming a SL. We will address this observation again later in the paper.

All of the samples were characterized by HR-XRD. A selection of the HR-XRD scans for samples ranging in the Mn

BEP fraction from 0.01 to 0.11 is shown in Figure 3a, where a sample containing 90% SLs is the top XRD scan. The expected position of the peaks for pure Sb_2Te_3 and pure MnSb_2Te_4 is also indicated at the bottom and top of the figure, respectively. The XRD scans are ordered by the Mn flux (BEP ratio) used during the growth of the samples, from the lowest Mn flux at the bottom to the highest at the top. The Mn BEP ratio used

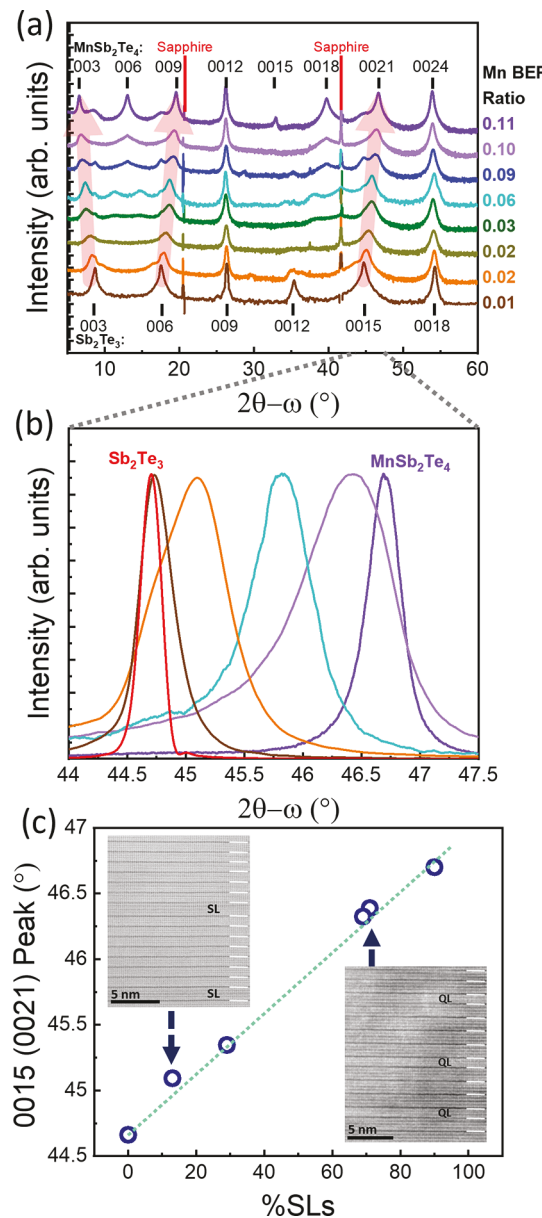


Figure 3. (a) HR-XRD measurements of samples grown with increasing Mn BEP Flux ratios. Peak positions for Sb_2Te_3 and MnSb_2Te_4 ¹³ are noted as black lines at the bottom and the top of the measurements, respectively. Mn BEP ratios for each sample are given in the same color as the sample scan to the right of the plots. (b) HR-XRD measurements of the region around the 0015 (Sb_2Te_3) to 0021 (MnSb_2Te_4) peaks of samples. The peak positions shift away from the position of Sb_2Te_3 as the Mn level increases, indicating the change in the crystal structure. (c) Peak position of the samples plotted as a function of their calculated %SLs from STEM (blue circles). A linear fit line, forced to go through 0% SLs, is plotted (aqua). Insets are the STEM images for the corresponding samples shown in Figure 2a (bottom right) and 2b (top left).

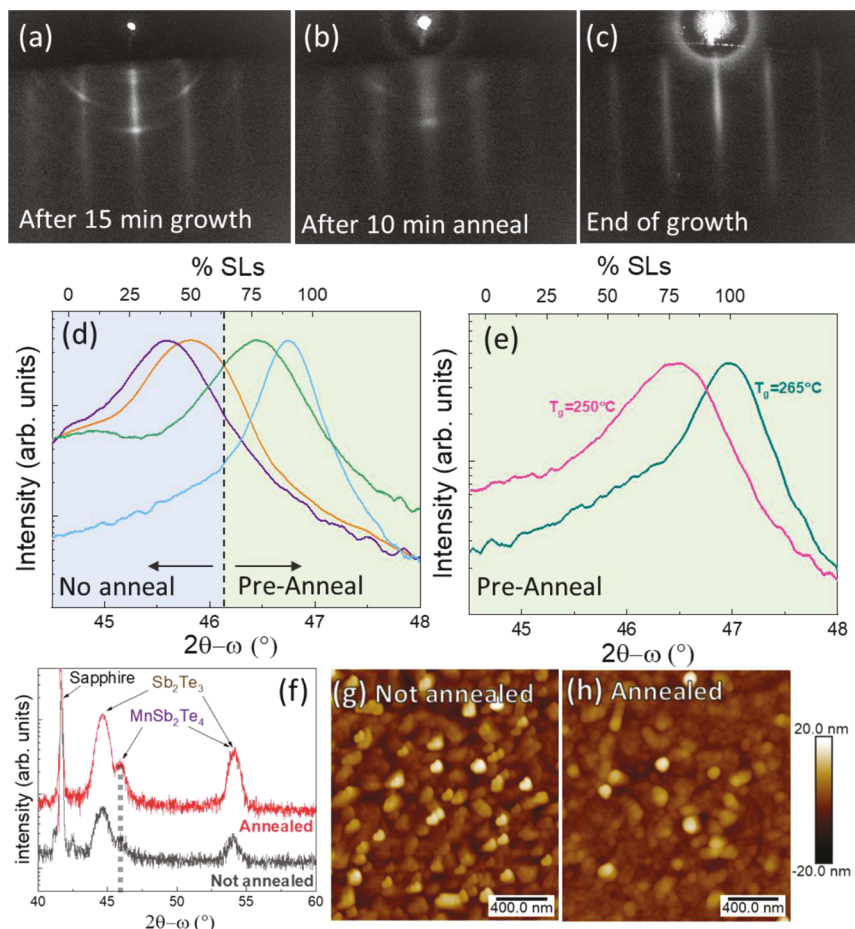


Figure 4. (a–c) In situ RHEED images of a sample surface before (a), and after (b) preannealing and (c) at the completion of the growth. (d) HR-XRD measurements of the 0015 (0021) peak of samples grown with (green, aqua) and without (purple, orange) the preannealing step. The blue and green shading distinguishes between the XRD peak positions for samples with the preannealing step (green) from those without (blue). (e) HR-XRD measurements of the 0015 (0021) peak of two samples grown with standard ($T_g = 250$ °C) and increased ($T_g = 265$ °C) growth temperatures. The green shading indicates that both samples in (e) were grown using the preannealing step. (f) HR-XRD scans of two thin layers grown for 15 min with (red) and without (black) a preannealing step. The peak position attributed to MnSb_2Te_4 (0021) is marked with a dotted line. (g,h) $2\ \mu\text{m} \times 2\ \mu\text{m}$ AFM images of the samples in (f). Both AFM images are based on the given scale bar.

during growth is given on the right of each scan. It is evident that as the Mn flux increases, there is a gradual change in the HR-XRD from that of a QL-based Sb_2Te_3 crystal structure to a MnSb_2Te_4 (SL-based) structure. At a low Mn BEP fraction (0.01–0.02), there is no change from Sb_2Te_3 in the peak positions of the XRD scan, meaning that at these low Mn fractions, the Mn is incorporated as a dopant rather than to form SLs. As the Mn BEP fraction increases, the peaks corresponding to the Sb_2Te_3 (003), (006), and (0015) planes show a clear shift, evolving into the (003), (009), and (0021) peaks of MnSb_2Te_4 , respectively, as can be seen by the red arrows superimposed on the plots. At intermediate Mn flux fractions (0.03–0.06), two weak peaks appear at around $2\theta - \omega \sim 10$ ° to 15°, as previously reported by others.¹⁵ Those authors proposed that this feature indicates a change of structure from Bi_2Te_3 to close to MnBi_4Te_7 . At the high Mn fraction levels (0.09–0.11), new single peaks that correspond closely to MnSb_2Te_4 (006) and (0018) planes appear. To further illustrate the gradual shift in the XRD peaks, Figure 3b shows an expanded view of the region around the (0015) plane of Sb_2Te_3 for a few selected samples. A clear trend is visible in the shift of the peak position as the Mn content increases, ranging from the Sb_2Te_3 (0015) peak position to the

MnSb_2Te_4 (0021) peak position. This shift is associated with the change in the crystal structure from pure Sb_2Te_3 to a superlattice of $(\text{Sb}_2\text{Te}_3)_{1-x}(\text{MnSb}_2\text{Te}_4)_x$ with varying x value. It is expected, based on Vegard's law, that in a thin-layer superlattice system, the XRD peak position will be given by the average composition of the structure.²⁵ A similar behavior can also be perceived upon careful observation of other reported XRD data of a related system, MnBi_2Se_4 , which also shows a gradual peak shift in XRD with increased Mn content.²⁶ Figure 3c shows the relationship between the shift of the HR-XRD (0015) peak and the %SL calculated from the STEM images. The calculated %SLs in the structure measured from the STEM images plotted as a function of the XRD peak position show a very good linear correlation, as expected based on the behavior described above. Thus, the shift in the XRD peak position is a direct measure of the %SL in the structure, and the linear fit of experimental data to Vegard's law, as given by eq 1, can be used to estimate the %SL in all of our samples based on the HR-XRD (0015) peak position ($2\theta - \omega$).

$$\begin{aligned}
 \%SL &= \frac{(2\theta - \omega)_{\text{Sample}} - (2\theta - \omega)_{\text{Sb}_2\text{Te}_3}}{0.023} \\
 &= \frac{(2\theta - \omega)_{\text{Sample}} - (2\theta - \omega)_{\text{Sb}_2\text{Te}_3}}{(2\theta - \omega)_{\text{MnSb}_2\text{Te}_4} - (2\theta - \omega)_{\text{Sb}_2\text{Te}_3}} \times 100 \\
 &\quad \text{Vegard's Law} \quad (1)
 \end{aligned}$$

This shift correlates with the increased presence of SLs in the samples; however, it is not an indication of the total Mn content in the sample because Mn is also incorporated as a dopant. We conclude that our samples grown under the conditions described above are Mn-rich and likely contain a fair amount of disorder in the form of Mn impurity concentration.

In an attempt to reduce the amount of disorder in the crystals, and to better understand the mechanism of Mn incorporation, a modified growth procedure was developed. Two changes were implemented. First, an annealing step was added after an initial thin portion of the layer was grown (from here on referred to as the *preannealing step*). Annealing has been used often in MBE and other growth techniques to improve crystalline quality.^{27–29} In our experiments, the sample growth began the same way as before, with the thin Sb_2Te_3 LTB followed by an interruption of the growth and the initiation of growth of the Mn-containing layer at the desired growth temperature (T_g). After 15 min, the growth is again stopped, and the sample temperature is raised to 300 °C for 10 min under a Te flux (*preannealing step*). The temperature is then lowered back to T_g and growth of the Mn-containing layer is resumed for the desired total growth time.

As a first assessment of the effect of the annealing step, we examined the evolution of the RHEED pattern. The RHEED image of the sample after 15 min of growth, but before the preannealing step (Figure 4a), often shows noticeable rings, suggesting some polycrystalline growth. After completing the 10 min. annealing step, the RHEED pattern typically improves (Figure 4b), showing less evidence of polycrystalline growth. Finally, at the end of the full layer growth, the RHEED improves significantly (Figure 4c). This suggests that the preannealing step is improving the crystalline quality of the initial thin layer. More importantly, implementation of the *preannealing step* had a significant effect on the portion of the sample that is grown over the preannealed thin layer. Figure 4d shows a comparison of the (0015) peak of the XRD scans of four samples, two grown with the *preannealing step* and two grown without it. All samples in Figure 4d were grown using a similar Mn flux fraction, T_g , and Te overpressure. The figure shows a clear shift toward a larger angle in the (0015) XRD peaks for the two samples grown with the *preannealing step*, suggesting that a larger %SL forms in the samples grown using the preannealed thin layer. The calculated %SLs for each sample of 4d, summarized in Table 1 as samples 1 through 4, increase from 40–50 %SLs without the *preannealing step* to 70–90 %SLs with the preannealed layer (samples 3 and 4), indicating that more of the Mn is incorporated in the form of SLs when the layer growth occurs over a thin preannealed layer, consequently reducing the incorporation of substitutional Mn impurities into the QLs and SLs.

In some samples, in addition to the *preannealing step*, the growth temperature (T_g) was also increased to 265–270 °C. The (0015) peak of the HR-XRD scans of two samples both grown with a *preannealing step* and the same value of Mn BEP,

Table 1. Calculated %SLs for Samples Grown under Different Growth Conditions

| Sample | Preannealed layer | Mn BEP ratio | T_g (°C) | %SLs |
|--|-------------------|--------------|------------|------|
| Effect of the preannealed layer (Figure 4a) | | | | |
| 1 | no | 0.060 | 260 | 41 |
| 2 | no | 0.060 | 255 | 51 |
| 3 | yes | 0.060 | 255 | 72 |
| 4 | yes | 0.065 | 255 | 92 |
| Effect of increased growth temperature (Figure 4b) | | | | |
| 5 | yes | 0.090 | 250 | 79 |
| 6 | yes | 0.090 | 265 | 100 |

but with two different T_g values of 250°C and 265 °C, are presented in Figure 4e. A further increase in the %SLs was observed for the sample grown at a higher growth temperature of 265 °C indicated by the shift of the (0015) XRD peak. The %SLs for these two samples, calculated from the XRD peak position, are given Table 1 as samples 5 and 6. Sample 6, grown at 265 °C, shows a further increase of the %SLs bringing its composition up to 100% SLs.

To understand the effect of the *preannealing step*, an experiment was performed in which we compared a thin layer grown for 15 min and annealed it for 10 min at 300 °C, and another thin layer was also grown for 15 min but not annealed. The HR-XRD of the two samples is shown in Figure 4f. The stronger and sharper XRD peaks for the annealed sample suggest improved crystallinity, consistent with the RHEED observations previously described. However, the positions of the (0015) peak for the two samples, identified by a dashed line in the figure, are the same, indicating the same %SL in both samples. The AFM images of the surfaces of the two samples (Figures 4g,h) show that the surface of the annealed sample (Figure 4h) is somewhat smoother (rms = 3.0 nm) than that of the sample (Figure 4g) that was not annealed (rms = 4.2 nm). The data of Figures 4f–h suggest that the *preannealing step* improves the crystalline quality of the annealed thin layer and makes its surface smoother, but it does not change the %SL of the thin annealed layer. Thus, we conclude that the increased %SLs obtained in the layer grown over the preannealed thin layer must be explained by a different mechanism not disclosed directly by our experiment.

The relationship between the Mn BEP fraction and the %SL of all the samples grown is illustrated in Figure 5a, which shows the samples grown using the original growth conditions as black open circles, the samples grown using the *preannealing step* as red open circles, and those grown using the *preannealing step* as well as a higher T_g as filled red circles. Within the range of MBE growth temperatures used here (250–270 °C), it can be assumed that all the Mn is incorporated into the layer (i.e., Mn will not reevaporate from the growth surface at these low growth temperatures). For the samples grown under the original growth conditions (black circles), there is a general correlation between the Mn BEP ratio and the XRD peak shift (or %SLs), but a large amount of scatter is present in the data. The scatter is consistent with our assertion that Mn is incorporated into the crystal in different ways and that a significant fraction of Mn is being incorporated as substitutional dopants without modifying the crystal structure (i.e., without forming SLs).

We also observe that the samples grown with the modified growth conditions, shown by the points in red, all have higher %SLs for the same Mn BEP ratio. This is consistent with our

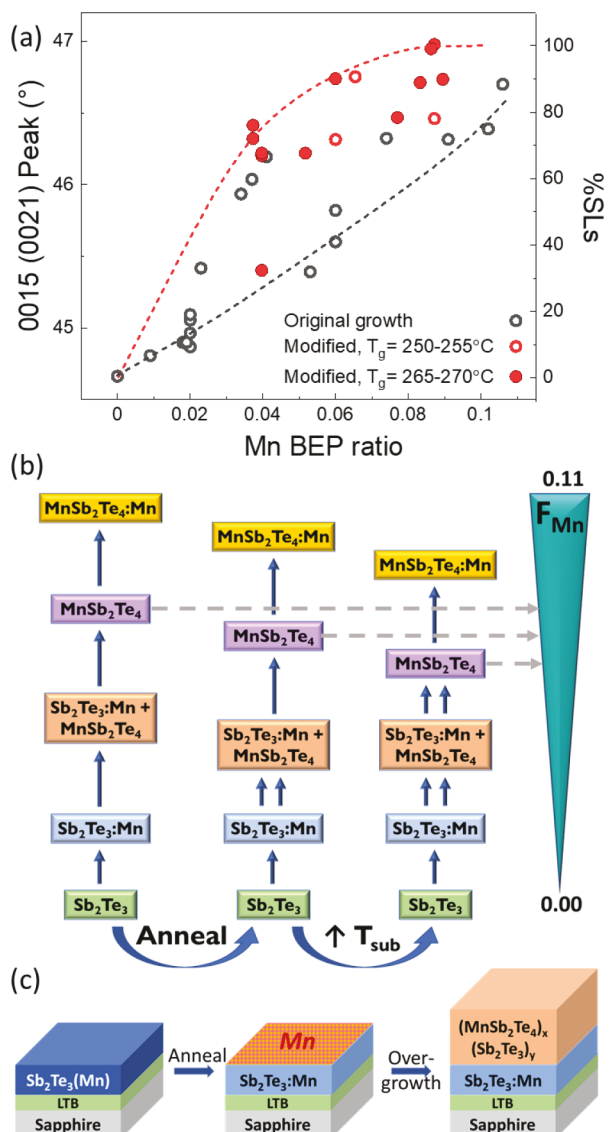


Figure 5. (a) Peak position (and %SLs) of all samples, as a function of the Mn BEP ratio. Samples grown under the original growth conditions are shown in black, while samples grown with the modified conditions are given in red: samples with the preannealing step only (red open circles) and those with preannealing step and increased growth temperatures (red filled circles). Black and red dashed lines represent the high and low boundaries of those data, highlighting the generally higher %SL obtained with the modified conditions. (b) Illustration of the proposed stepwise growth process for the material formed as a function of increasing Mn flux ratios (F_{Mn} , green cone), and the changes that the two modification steps used, preannealing step and increased growth temperatures, produce on the growth. The gray arrows indicate the lower Mn flux needed to achieve stoichiometric MnSb_2Te_4 when the growth modification steps are introduced. (c) Schematic of the sample structure as it undergoes the changes introduced by the preannealing step in the proposed mechanism.

conclusion that the *preannealing step* promotes the formation of SLs in the subsequent layer, rather than its incorporation into the lattice as a dopant. Within the red data points, the samples grown at a higher T_g , illustrated by the filled red circles, typically result in even higher %SLs for the same Mn BEP during growth.

Our observations are summarized schematically in Figure 5b. The Mn BEP ratio (proportional to the Mn flux ratio F_{Mn}) used during growth is illustrated by the green cone on the right, increasing from values of 0.00 to 0.11 in our growths. At very low Mn BEP ratios, only Sb_2Te_3 QLs doped with Mn ($\text{Sb}_2\text{Te}_3:\text{Mn}$) can form. As more Mn is added during growth, (as the Mn BEP ratio increases), SLs can be formed resulting in mixed QL and SL structures, with a higher %SL as the Mn BEP ratio increases. The implementation of a *preannealing step* results in SLs formed at a lower Mn BEP ratio. This is illustrated by the dashed gray arrows, which indicates the relative Mn flux fraction at which stoichiometric MnSb_2Te_4 will form. Based on these observations, we propose the following tentative mechanism, depicted in Figure 5c. We assume that, in MBE growth, a critical quantity of excess Mn atoms must be present at the surface of the sample in order for Mn to form a SL rather than incorporate as impurities into the QLs. With a very low Mn BEP ratio, Mn is incorporated only as a substitutional impurity (Figure 5c left frame). As the Mn BEP ratio increases, the Mn is incorporated into the QL as impurity atoms and some excess Mn accumulates on the growing surface until there is a sufficient excess Mn on the surface to form SLs. We propose that the *preannealing step* facilitates the accumulation of Mn on the surface instead of incorporating as an impurity into the Sb_2Te_3 layer (Figure 5c middle frame), thus favoring the formation of SLs at lower Mn BEP ratios as compared to when no *preannealing step* is performed. Once this excess Mn is produced, it is more likely for an excess of Mn to remain on the surface as the layers grow, promoting the formation of SLs throughout the growth (Figure 5c right frame).

The effect of increasing the growth temperature is also illustrated in Figure 5b. An increase in the %SL formation for the same Mn BEP fraction is also observed by the use of a higher T_g . The reason for this enhancement might also be related to the ease of Mn accumulation on the surface at a higher temperature, because at a higher temperature Sb may desorb from the surface leading to a higher Mn concentration. However, the growth temperature effect may also be due to the higher formation energy of MnSb_2Te_4 ,³⁰ which may be favored at higher T_g .

The presence and the location of the excess Mn in our samples can be further ascertained from detailed STEM analysis. The HAADF STEM image for a sample with 72% SLs is shown in Figure 6a. The Mn content in this sample of $\sim 21\%$, measured by EDX, suggests that there is significant excess Mn in the lattice, as seen in the previous samples. To determine the location of the excess Mn in the crystal, intensity profile measurements of the HAADF TEM images were performed. Because of their smaller atomic mass, Mn atoms are darker in these images compared to the Sb and Te atoms, which are both of similar higher brightness. Figure 6b, an intensity line scan along the growth direction, shows a combination of SLs evident from a sequence of seven intensity peaks, one for each atomic plane, and QLs, evident from the presence of five peaks corresponding to the five atomic planes. The peak corresponding to the middle layer in the SLs has a lower intensity because of the small mass of the Mn atoms, suggesting predominantly Mn in that layer, as expected, whereas other peaks, corresponding to Sb and Te, are higher in intensity. The QLs show similarly high intensity for all the peaks, as expected from the closely similar atomic mass of Te and Sb. However, careful attention to the Te and Sb peaks in these layers

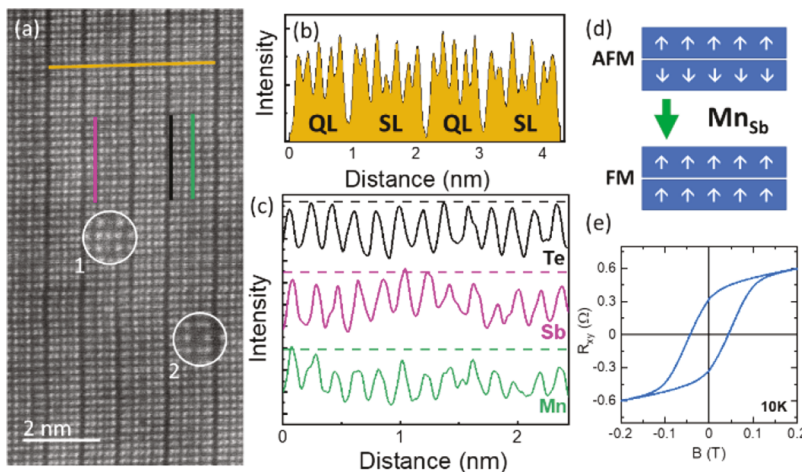


Figure 6. STEM analysis of a sample with 72% SLs; (a) HAADF STEM image of the sample. Inset circles 1 and 2; high-resolution STEM image showing antisites seen as brighter dots (Sb) in the Mn atomic layers (center of circle 1) and dark dots (Mn) in the Sb atomic layers (center of circle 2). (b) Image intensity profile along the growth direction showing SLs and QLs. The yellow line indicates the location of the scan. (c) Intensity profiles along the atomic planes of Te (black line), Sb (magenta line), and Mn (green line) showing large variations in the Sb and Mn lines suggesting the presence of Mn–Sb atom exchange or antisites. (d) Illustration of the ferromagnetic alignment of MnSb₂Te₄ SL produced by the presence of Mn_{Sb} antisites. (e) Hysteresis loop of the Hall resistance R_{xy} as a function of the magnetic field, B , measured at 10 K showing ferromagnetic behavior for this sample.

suggests some intensity variations within each atomic plane. To further quantify this, Figure 6c shows three intensity line scans along the Te, Sb and Mn planes, respectively. All intensity scans were taken from Figure 6a and are color coded in the location where they were taken. While the peaks along the Te plane have relatively uniform intensities, significant variations in peak intensity are present along the Sb and Mn line scans. These variations can be understood from the presence of Mn atoms in Sb sites, leading to reduced intensities of the Sb planes, and Sb atoms in the Mn sites leading to higher intensities of the Mn planes. Further evidence of these atomic exchanges is seen in the zoomed-in circles in Figure 6a, which show the presence of “bright” atoms in the Mn sites (circle 1) as well as “dark” atoms in the Sb sites (circle 2).

Ferromagnetism in Mn-rich MnSb₂Te₄ has been recently reported and has been attributed to Mn–Sb site exchange inducing ferromagnetic coupling between stacked SLs (see Figure 6d).¹⁰ Hall resistance (R_{xy}) plots as a function of magnetic field of our samples reveal that all our samples having at least a few %SLs exhibit ferromagnetic behavior, as demonstrated by the presence of a hysteresis loop near ~ 0 T magnetic field (B). In particular, the R_{xy} vs B hysteresis plot for the sample of 6a, demonstrating its ferromagnetic behavior, is shown in Figure 6e. We suggest that the ferromagnetic behavior of our MnSb₂Te₄ may also be due to Mn–Sb site exchange. A detailed investigation of the magnetic properties of our samples is currently underway and is beyond the scope of this paper.

CONCLUSIONS

In this work, we have investigated the growth by MBE of $(\text{Sb}_2\text{Te}_3)_{1-x}(\text{MnSb}_2\text{Te}_4)_x$ structures on sapphire substrates. Increasing the flux fraction of Mn (or Mn BEP ratio) during growth results in a gradual change of the composition of the structure from all Sb_2Te_3 QLs ($x = 0$) to all MnSb₂Te₄ SLs ($x = 1$). The Mn content in excess of that indicated by the percent (%) of SLs suggests that Mn is also incorporated as a dopant forming $\text{Sb}_2\text{Te}_3:\text{Mn}$ and $\text{MnSb}_2\text{Te}_4:\text{Mn}$. We conclude

that under our initial growth conditions, adjusting the Mn BEP ratio during growth is not sufficient to accurately determine the resulting $(\text{Sb}_2\text{Te}_3)_{1-x}(\text{MnSb}_2\text{Te}_4)_x$ structure and the large degree of excess Mn incorporated into the layers.

We also analyzed the evolution of the XRD scans of the layers as the Mn content is increased. The results show a gradual shift of several peaks from the Sb_2Te_3 position to the corresponding MnSb₂Te₄ position. We show that this peak shift can be used to accurately calculate the %SLs in the resulting crystal.

Modifying the growth conditions by the incorporation of a *preannealing step* at the beginning of growth, a significant increase in the %SLs formed for the same Mn BEP ratio used during growth was observed. This showed that with the preannealed layer, the incorporation of Mn as a structural element to form SLs is favored rather than its incorporation as an impurity. We propose a mechanism consistent with our observations based on the assumption that a local excess of Mn is needed at the growth surface for the formation of SLs during growth. We suggest that the formation of a Mn-rich growth surface is facilitated by the *preannealing step*. A further increase in the %SLs for the same Mn BEP fraction was observed by also increasing the growth temperature, possibly because of a similar effect. The insights obtained through our experiments into the MBE growth process of these magnetic TIs are essential for the eventual development of precisely controlled on-demand layered structures of these materials.

Measurements of the Hall resistance as a function of magnetic field of our samples show that the samples are ferromagnetic, which may be in part due to the excess Mn incorporation into our layers. We present a HAADF TEM image intensity profile measurement that gives evidence of substitution of Mn in Sb sites, as well as Sb in Mn sites. Mn/Sb antisites in MnSb₂Te₄ have been reported to lead to ferromagnetic behavior. The demonstrated control of the QL to SL ratios and of the excess Mn incorporation into our samples achieved by modifying the growth conditions should enable the fabrication of these highly promising and

technologically relevant materials with precisely tailored magnetic properties.

■ AUTHOR INFORMATION

Corresponding Author

Maria C. Tamargo — Department of Chemistry, The City College of New York, New York, New York 10031, United States; Ph.D. Program in Chemistry, The Graduate Center of the City University of New York, New York, New York 10016, United States;  orcid.org/0000-0002-2991-2674; Email: mtamargo@ccny.cuny.edu

Authors

Ido Levy — Department of Chemistry, The City College of New York, New York, New York 10031, United States; Ph.D. Program in Chemistry, The Graduate Center of the City University of New York, New York, New York 10016, United States;  orcid.org/0000-0002-3962-4393

Candice Forrester — Department of Chemistry, The City College of New York, New York, New York 10031, United States; Ph.D. Program in Chemistry, The Graduate Center of the City University of New York, New York, New York 10016, United States

Haiming Deng — Department of Physics, The City College of New York, New York, New York 10031, United States; Ph.D. Program in Physics, The Graduate Center of the City University of New York, New York, New York 10016, United States

Manuel Roldan-Gutierrez — Eyring Materials Center, Arizona State University, Tempe, Arizona 85287, United States

Martha R. McCartney — Department of Physics, Arizona State University, Tempe, Arizona 85287, United States

David J. Smith — Department of Physics, Arizona State University, Tempe, Arizona 85287, United States;

 orcid.org/0000-0002-8810-4386

Christophe Testelin — Sorbonne Université, CNRS, Institut des NanoSciences de Paris, F-75005 Paris, France

Lia Krusin-Elbaum — Department of Physics, The City College of New York, New York, New York 10031, United States; Ph.D. Program in Physics, The Graduate Center of the City University of New York, New York, New York 10016, United States

Complete contact information is available at:

<https://pubs.acs.org/10.1021/acs.cgd.1c01453>

Notes

The authors declare no competing financial interest.

■ ACKNOWLEDGMENTS

This work was supported by NSF Grant No. DMR-2011738 (PAQM). Partial support is also acknowledged from NSF Grant Nos. HRD-1547830 (CREST IDEALS) and HRD-2112550 (Phase II CREST IDEALS). The authors would like to acknowledge the Nanofabrication Facility of the CUNY Advanced Science Research Center (ASRC) for instrument use and scientific and technical assistance.

■ REFERENCES

- (1) Yu, R.; Zhang, W.; Zhang, H. J.; Zhang, S. C.; Dai, X.; Fang, Z. Quantized Anomalous Hall Effect in Magnetic Topological Insulators. *Science* **2010**, *329*, 61–64.
- (2) Chang, C. Z.; Zhang, J.; Feng, X.; Shen, J.; Zhang, Z.; Guo, M.; Li, K.; Ou, Y.; Wei, P.; Wang, L. L.; Ji, Z. Q.; Feng, Y.; Ji, S.; Chen, X.; Jia, J.; Dai, X.; Fang, Z.; Zhang, S. C.; He, K.; Wang, Y.; Lu, L.; Ma, X. C.; Xue, Q. K. Experimental Observation of the Quantum Anomalous Hall Effect in a Magnetic Topological Insulator. *Science* **2013**, *340*, 167–170.
- (3) Chang, C. Z.; Zhang, J.; Liu, M.; Zhang, Z.; Feng, X.; Li, K.; Wang, L. L.; Chen, X.; Dai, X.; Fang, Z.; Qi, X. L.; Zhang, S. C.; Wang, Y.; He, K.; Ma, X. C.; Xue, Q. K. Thin Films of Magnetically Doped Topological Insulator with Carrier-Independent Long-Range Ferromagnetic Order. *Adv. Mater.* **2013**, *25*, 1065–1070.
- (4) Checkelsky, J. G.; Yoshimi, R.; Tsukazaki, A.; Takahashi, K. S.; Kozuka, Y.; Falson, J.; Kawasaki, M.; Tokura, Y. Trajectory of the Anomalous Hall Effect Towards the Quantized State in a Ferromagnetic Topological Insulator. *Nat. Phys.* **2014**, *10*, 731–736.
- (5) Mogi, M.; Yoshimi, R.; Tsukazaki, A.; Yasuda, K.; Kozuka, Y.; Takahashi, K. S.; Kawasaki, M.; Tokura, Y. Magnetic Modulation Doping in Topological Insulators Toward Higher-Temperature Quantum Anomalous Hall Effect. *Appl. Phys. Lett.* **2015**, *107*, 182401.
- (6) Ou, Y.; Liu, C.; Jiang, G.; Feng, Y.; Zhao, D.; Wu, W.; Wang, X. X.; Li, W.; Song, C.; Wang, L. L.; Wang, W.; Wu, W.; Wang, Y.; He, K.; Ma, X. C.; Xue, Q. K. Enhancing the Quantum Anomalous Hall Effect by Magnetic Codoping in a Topological Insulator. *Adv. Mater.* **2018**, *30*, No. 1703062.
- (7) Lee, D. S.; Kim, T. H.; Park, C. H.; Chung, C. Y.; Lim, Y. S.; Seoa, W. S.; Park, H. H. Crystal Structure, Properties and Nanostructuring of a new Layered Chalcogenide Semiconductor, Bi_2MnTe_4 . *CrystEngComm* **2013**, *15*, 5532–5538.
- (8) Deng, Y.; Yu, Y.; Shi, M. Z.; Guo, Z.; Xu, Z.; Wang, J.; Chen, X. H.; Zhang, Y. Quantum Anomalous Hall Effect in Intrinsic Magnetic Topological Insulator MnBi_2Te_4 . *Science* **2020**, *367*, 895–900.
- (9) Deng, H.; Chen, Z.; Wołos, A.; Konczykowski, M.; Sobczak, K.; Sitnicka, J.; Fedorchenko, I. V.; Borysiuk, J.; Heider, T.; Pluciński, L.; Park, K.; Georgescu, A. B.; Cano, J.; Krusin-Elbaum, L. High-Temperature Quantum Anomalous Hall Regime in a $\text{MnBi}_2\text{Te}_4/\text{Bi}_2\text{Te}_3$ Superlattice. *Nat. Phys.* **2021**, *17*, 36–42.
- (10) Riberolles, S. X. M.; Zhang, Q.; Gordon, E.; Butch, N. P.; Ke, L.; Yan, J. Q.; McQueeney, R. J. Evolution of Magnetic Interactions in Sb-Substituted MnBi_2Te_4 . *Phys. Rev. B* **2021**, *104*, No. 064401.
- (11) Liu, Y.; Wang, L. L.; Zheng, Q.; Huang, Z.; Wang, X.; Chi, M.; Wu, Y.; Chakoumakos, B. C.; McGuire, M. A.; Sales, B. C.; Wu, W.; Yan, J. Site Mixing for Engineering Magnetic Topological Insulators. *Phys. Rev. X* **2021**, *11*, No. 021033.
- (12) Wimmer, S.; Sánchez-Barriga, J.; Küppers, P.; Ney, A.; Schierle, E.; Freyse, F.; Caha, O.; Michalička, J.; Liebmann, M.; Primetzhofer, D.; Hoffman, M.; Ernst, A.; Otrókov, M. M.; Bihlmayer, G.; Weschke, E.; Lake, B.; Chulkov, E. V.; Morgenstern, M.; Bauer, G.; Springholz, G.; Rader, O. Mn-Rich MnSb_2Te_4 : A Topological Insulator with Magnetic Gap Closing at High Curie Temperatures of 45–50 K. *Adv. Mater.* **2021**, *33*, No. 2102935.
- (13) Li, H.; Li, Y.; Lian, Y.; Xie, W.; Chen, L.; Zhang, J.; Wu, Y.; Fan, S. Glassy Magnetic Ground State in Layered Compound MnSb_2Te_4 . *Sci. China Mater.* **2021**, *477*.
- (14) Murakami, T.; Nambu, Y.; Koretsune, T.; Xiangyu, G.; Yamamoto, T.; Brown, C. M.; Kageyama, H. Realization of Interlayer Ferromagnetic Interaction in MnSb_2Te_4 Toward the Magnetic Weyl Semimetal State. *Phys. Rev. B* **2019**, *100*, 194103.
- (15) Lapano, J.; Nuckols, L.; Mazza, A. R.; Pai, Y. Y.; Zhang, J.; Lawrie, B.; Moore, R. G.; Eres, G.; Lee, H. N.; Du, M. H.; Ward, T. Z.; Lee, J. S.; Weber, W. J.; Zhang, Y.; Brahlek, M. Adsorption-Controlled Growth of $\text{MnTe}(\text{Bi}_2\text{Te}_3)_n$ by Molecular Beam Epitaxy Exhibiting Stoichiometry-Controlled Magnetism. *Phys. Rev. Mater.* **2020**, *4*, No. 111201.
- (16) Kagerer, P.; Fornari, C. I.; Buchberger, S.; Morelhao, S. L.; Vidal, R. C.; Tcakaev, A.; Zabolotnyy, V.; Weschke, E.; Hinkiv, V.; Kamp, M.; Büchner, B.; Isaeva, A.; Bentmann, H.; Reinertet, F. Molecular Beam Epitaxy of Antiferromagnetic $(\text{MnBi}_2\text{Te}_4)(\text{Bi}_2\text{Te}_3)$ Thin Films on $\text{BaF}_2(111)$. *J. Appl. Phys.* **2020**, *128*, 135303.
- (17) Trang, C. X.; Li, Q.; Yin, Y.; Hwang, J.; Akhgar, G.; Bernardo, I. D.; Grubišić-Čabo, A.; Tadich, A.; Fuhrer, M. S.; Mo, S. K.; Medhekar, N. V.; Edmonds, M. T. Crossover from 2D Ferromagnetic

Insulator to Wide Band Gap Quantum Anomalous Hall Insulator in Ultrathin MnBi_2Te_4 . *ACS Nano* **2021**, *15*, 13444–13452.

(18) Rienks, E. D. L.; Wimmer, S.; Sánchez-Barriga, J.; Caha, O.; Mandal, P. S.; Růžička, J.; Ney, A.; Steiner, H.; Volobuev, V. V.; Groiss, H.; Albu, M.; Kothleitner, G.; Michalička, J.; Khan, S. A.; Minár, J.; Ebert, H.; Bauer, G.; Freyse, F.; Varykhalov, A.; Rader, O.; Springholz, G. Large Magnetic Gap at the Dirac Point in $\text{Bi}_2\text{Te}_3/\text{MnBi}_2\text{Te}_4$ Heterostructures. *Nature* **2019**, *576*, 423–428.

(19) Hirahara, T.; Eremeev, S. V.; Shirasawa, T.; Okuyama, Y.; Kubo, T.; Nakanishi, R.; Akiyama, R.; Takayama, A.; Hajiri, T.; Ideta, S.; Matsunami, M.; Sumida, K.; Miyamoto, K.; Takagi, Y.; Tanaka, K.; Okuda, T.; Yokoyama, T.; Kimura, S.; Hasegawa, S.; Chulkov, E. V. Large-Gap Magnetic Topological Heterostructure Formed by Subsurface Incorporation of a Ferromagnetic Layer. *Nano Lett.* **2017**, *17*, 3493–3500.

(20) Hirahara, T.; Otrokov, M. M.; Sasaki, T. T.; Sumida, K.; Tomohiro, Y.; Kusaka, S.; Okuyama, Y.; Ichinokura, S.; Kobayashi, M.; Takeda, Y.; Amemiya, K.; Shirasawa, T.; Ideta, S.; Miyamoto, K.; Tanaka, K.; Kuroda, S.; Okuda, T.; Hono, K.; Eremeev, S. V.; Chulkov, E. V. Fabrication of a Novel Magnetic Topological Heterostructure and Temperature Evolution of its Massive Dirac Cone. *Nat. Commun.* **2020**, *11*, 4821.

(21) Zhao, Y. F.; Zhou, L. J.; Wang, F.; Wang, G.; Song, T.; Ovchinnikov, D.; Yi, H.; Mei, R.; Wang, K.; Chan, M. H. W.; Liu, C. X.; Xu, X.; Chang, C. Z. Even–Odd Layer-Dependent Anomalous Hall Effect in Topological Magnet MnBi_2Te_4 Thin Films. *Nano Lett.* **2021**, *21*, 7691–7698.

(22) Chen, P.; Yao, Q.; Sun, Q.; Grutter, A. J.; Quarterman, P.; Balakrishnan, P. P.; Kinane, C. J.; Caruana, A. J.; Langridge, S.; Cui, B.; Li, L.; Ji, Y.; Zhang, Y.; Liu, Z.; Zou, J.; Yu, G.; Yang, Y.; Kou, X. Tailoring Magnetic Exchange Interactions in Ferromagnet-Intercalated MnBi_2Te_4 Superlattices. <https://arxiv.org/abs/2112.04303>.

(23) Bansal, N.; Kim, Y. S.; Edrey, E.; Brahmek, M.; Horibe, Y.; Iida, K.; Tanimura, M.; Li, G. H.; Feng, T.; Lee, H. D.; Gustafsson, T.; Andrei, E.; Oh, S. Epitaxial Growth of Topological Insulator Bi_2Se_3 Film on Si(111) with Atomically Sharp Interface. *Thin Solid Films* **2011**, *520*, 224–229.

(24) Bansal, N.; Kim, Y. S.; Brahmek, M.; Edrey, E.; Oh, S. Thickness-Independent Transport Channels in Topological Insulator Bi_2Se_3 Thin Films. *Phys. Rev. Lett.* **2012**, *109*, No. 116804.

(25) Vickers, M. E.; Kappers, M. J.; Smeeton, T. M.; Thrush, E. J.; Barnard, J. S.; Humphreys, J. S. Determination of the indium content and layer thicknesses in InGaN/GaN quantum wells by X-ray scattering. *J. Appl. Phys.* **2003**, *94*, 1565–1574.

(26) Hagmann, J. A.; Li, X.; Chowdhury, S.; Dong, S. N.; Rouvimov, R.; Pookpanratana, S. J.; Yu, K. M.; Orlova, T. A.; Bolin, T. B.; Segre, C. U.; Seiler, D. G.; Richter, C. A.; Liu, X.; Dobrowolska, M.; Furdyna, J. K. Molecular Beam Epitaxy Growth and Structure of Self-Assembled $\text{Bi}_2\text{Se}_3\text{-Bi}_2\text{MnSe}_4$ multilayer heterostructures. *New J. Phys.* **2017**, *19*, No. 085002.

(27) Lee, J. W.; Shichijo, H.; Tsai, H. I.; Matyi, R. J. Defect Reduction by Thermal Annealing of GaAs Layers Grown by Molecular Beam Epitaxy on Si Substrates. *Appl. Phys. Lett.* **1987**, *50*, 31–33.

(28) Guo, X.; Xu, Z. J.; Liu, H. C.; Zhao, B.; Dai, X. Q.; He, H. T.; Wang, J. N.; Liu, H. J.; Ho, W. K.; Xie, M. H. Single Domain Bi_2Se_3 Films Grown on InP(111)A by Molecular Beam Epitaxy. *Appl. Phys. Lett.* **2013**, *102*, 151604.

(29) Gong, Y.; Guo, J.; Li, J.; Zhu, K.; Liao, M.; Liu, X.; Zhang, Q.; Gu, L.; Tang, L.; Feng, X.; Zhang, D.; Li, W.; Song, C.; Wang, L.; Yu, P.; Chen, X.; Wang, Y.; Yao, H.; Duan, W.; Xu, Y.; Zhang, S. C.; Ma, X.; Xue, Q. K.; He, K. Experimental Realization of an Intrinsic Magnetic Topological Insulator. *Chin. Phys. Lett.* **2019**, *36*, No. 076801.

(30) Du, M. H.; Yan, J.; Cooper, V. R.; Eisenbach, M. Tuning Fermi Levels in Intrinsic Antiferromagnetic Topological Insulators MnBi_2Te_4 and MnBi_4Te_7 by Defect Engineering and Chemical Doping. *Adv. Funct. Mater.* **2021**, *31*, No. 2006516.

Recommended by ACS

Probing a Proximity-Coupling-Induced Hybrid Anomalous Hall Effect in Epitaxial $\text{MnBi}_2\text{Te}_4/\text{Bi}_2\text{Te}_3$ Nanostructures

Cheng Li, Tian Jiang, *et al.*

JULY 26, 2022

ACS APPLIED NANO MATERIALS

READ 

Unconventional Pressure-Driven Metamagnetic Transitions in Topological van der Waals Magnets

Tiema Qian, Ni Ni, *et al.*

JUNE 22, 2022

NANO LETTERS

READ 

Crossover from 2D Ferromagnetic Insulator to Wide Band Gap Quantum Anomalous Hall Insulator in Ultrathin MnBi_2Te_4

Chi Xuan Trang, Mark T. Edmonds, *et al.*

AUGUST 13, 2021

ACS NANO

READ 

Thickness-Driven Quantum Anomalous Hall Phase Transition in Magnetic Topological Insulator Thin Films

Yuchen Ji, Xufeng Kou, *et al.*

JANUARY 10, 2022

ACS NANO

READ 

Get More Suggestions >